Biosensors and Bioelectronics 303 (2026) 118567

Contents lists available at ScienceDirect

Biosensors and Bioelectronics

journal homepage: www.elsevier.com/locate/bios

An electrochemical enzyme-linked immunosorbent assay for interleukin 18 quantification in 3D skin models derived from ALS patients

Nicola Furlan [a], Ugo D'Amora [b], Ines Fasolino [b,*], Alessandro Silvestri [a,**], Chiara Zanardi [a,c]

[a] Department of Molecular Sciences and Nanosystems, Ca' Foscari University of Venice, Venezia, 30170, Italy
[b] Institute of Polymers, Composites and Biomaterials – National Research Council (IPCB-CNR), Viale Kennedy 54, Mostra d'Oltremare pad. 20, Naples, 80125, Italy
[c] Institute of Organic Synthesis and Photoreactivity - National Research Council of Italy, Bologna, 40129, Italy

ARTICLE INFO

Keywords:
Electrochemical Enzyme-Linked Immunosorbent Assays (e-ELISA)
Amyotrophic lateral sclerosis (ALS)
3D skin model
Interleukin 18 (IL-18)

ABSTRACT

Amyotrophic lateral sclerosis (ALS) is a devastating neurodegenerative disorder that currently lacks validated molecular biomarkers for early diagnosis and prognosis, severely delaying personalized care. Interleukin 18 (IL-18), a proinflammatory cytokine linked to NLRP-3 inflammasome activation, has emerged as a promising biomarker for ALS. However, traditional colorimetric Enzyme-Linked Immunosorbent Assays (ELISAs) lack the sensitivity to distinguish IL-18 levels between Fast- and Slow-progressing ALS patients. To overcome this, we developed a highly sensitive electrochemical ELISA (e-ELISA) test by systematically optimizing key parameters, including the capture antibody immobilization strategy, the electrochemical mediator, and reagent concentrations. We then applied the optimized e-ELISA protocol to quantify IL-18 in 3D innervated skin models constructed using 3D-printed methacrylated hyaluronic acid (MeHA) and electrospun polylactic acid (PLLA) fibers, and colonized with patient-derived fibroblasts and neuronal cells. Reaching a limit of detection of 1.77 pg×mL^{-1}, the e-ELISA not only differentiated ALS models from the healthy control but, most critically, distinguished between a Fast- and a Slow-progressing ALS models based on significantly different IL-18 concentrations. By discriminating IL-18 levels in biologically representative models, this work validates the developed high-performance e-ELISA for personalized clinical use, providing a foundation for the design of portable diagnostic devices.

1. Introduction

Amyotrophic lateral sclerosis (ALS) is a rare and rapidly progressive neurodegenerative disorder where diagnosis is often delayed by symptomatic heterogeneity and a lack of specific biomarkers (Downer et al., 2023). Current protocols rely on exclusionary clinical exams, electromyography, and neuroimaging, which fail to distinguish between Fast and Slow disease progression early on (Irwin et al., 2024). This absence of validated molecular markers hinders both personalized care and the development of effective therapeutic strategies.

Interleukin 18 (IL-18) has been recently investigated as a promising biomarker for ALS as a specific sign of inflammasome cascade activation. Indeed, recent findings revealed that NLRP-3 (NOD-, LRR- and pyrin domain-containing protein 3), a component of the inflammasome cascade, is involved in ALS pathogenesis and constitutes a biomarker for predicting ALS onset and progression in ALS patients (Scarpa et al., 2026). An upregulated inflammatory response in neurodegenerative disorders determines the release of proinflammatory cytokines, which play a pivotal role in the induction of neuroinflammation (Treccani et al., 2025). Furthermore, NLRP-3, through the activation of Caspase-1, promotes the maturation of the pro-inflammatory cytokines, including IL-18 (Deora et al., 2020).

Another important drawback hindering ALS diagnosis is that the central nervous system (CNS) is accessible only *post-mortem*, meanwhile biopsies are highly invasive. Previous studies highlighted that cutaneous nerve degeneration detected in skin biopsies of ALS patients mimics neurodegenerative mechanisms acting at the CNS (Nolano et al., 2024). However, even if skin is a more accessible organ, its biopsy remains an invasive procedure because it requires multiple tissue removals and the use of local anesthesia, thus leading to reduced patient compliance.

This article is part of a special issue entitled: Biosensors 2025 published in Biosensors and Bioelectronics.

[*] Corresponding author.

[**] Corresponding author.

E-mail addresses: ines.fasolino@cnr.it (I. Fasolino), alessandro.silvestri@unive.it (A. Silvestri).

https://doi.org/10.1016/j.bios.2026.118567
Received 5 December 2025; Received in revised form 22 February 2026; Accepted 26 February 2026

To overcome this limitation, Fasolino and coworkers developed a 3D innervated skin model by combining 3D printing of methacrylated hyaluronic acid (MeHA) for better reproducing dermis/epidermis and electrospinning of polylactic acid (PLLA) for mimicking skin innervation (Scarpa et al., 2026). This 3D skin tissue model colonized with cells, directly isolated from patients' skin (ALS Slow and Fast progressors-derived fibroblasts), provided an efficient tool useful to study ALS disease (Scarpa et al., 2026). Indeed, the artificial 3D skin model allowed to detect NLRP-3 inflammasome-mediated activation in ALS Slow and Fast progressors-derived fibroblasts and pyroptosis-related cytokines in artificial interstitial fluid (ISF) produced after cell-colonization. The study performed on this 3D skin model revealed that Slow and Fast ALS progressors released higher IL-18 levels than healthy controls by ELISA kit assay, thus suggesting IL-18 may represent a specific diagnostic marker of ALS disease (Scarpa et al., 2026). However, the sensitivity of the colorimetric enzyme-linked immunosorbent assay (ELISA) did not allow for distinguishing Fast from Slow progressing patients (Scarpa et al., 2026).

The solution to overcome this limitation could reside in the use of electrochemical ELISAs (e-ELISAs), which are a promising alternative to traditional optical ELISAs. e-ELISA could guarantee improved sensitivity and limits of detection (Arya and Estrela, 2018; Milne et al., 2024; Zhang et al., 2019). Furthermore, e-ELISA could be easily integrated with miniaturized and portable electrical instrumentation (Arya and Estrela, 2020; Sajeevan et al., 2025; Singh et al., 2024). Indeed, e-ELISAs replace the conventional colorimetric measurement with an electrochemical readout, such as cyclic voltammetry or chronoamperometry. This allows the enzymatic reaction to be directly converted into a measurable electrical signal. These advantages make e-ELISAs a transformative technology for translating laboratory breakthroughs into practical diagnostic solutions.

However, to fully exploit the potential of electrochemical ELISA, it is mandatory to improve its analytical performance to achieve the necessary sensitivity and LOD required for clinical diagnosis. Despite the established advantages of e-ELISAs and the numerous studies in the literature, a significant knowledge gap persists. There is a lack of systematic studies on how the individual components of these assays collectively influence their overall analytical performance. This fragmented approach hinders the full realization of e-ELISA's potential.

The present work aims to provide a systematic and comprehensive evaluation of key parameters for optimization of e-ELISA, to achieve LOD and sensitivities that could allow the distinction of a Fast-progressing ALS patient from a Slow-progressing patient by quantifying the level of IL-18 produced by their fibroblasts. Our study specifically investigates crucial factors, including the immobilization strategy of the capture antibody (cAb), the optimal orientation on the surface, the selection of the most effective electrochemical mediator, and the precise optimization of reagent ratios and all the experimental steps. We used Human Immunoglobulin G (IgG), a benchmark analyte, to develop the e-ELISA. We then leveraged the acquired knowledge to develop an e-ELISA for detecting IL-18. Hence, we utilized the optimized assay to quantify IL-18 in 3D skin models colonized by fibroblast cells isolated from ALS patients. The assay effectively differentiated ALS-positive models from controls and, importantly, it distinguished between patients with Fast and Slow disease progression. This finding highlights the practical value of our method and underscores the significant potential of our optimization approach in clinical applications.

2. Materials and methods

2.1. Electrochemical tests

Cyclic voltammetric (CV) responses were recorded at carbon screen printed electrode (CSPE), in 0.1 M of phosphate buffer solution (PBS; pH 7) also containing 0.1 M KCl, 2 mM H_2O_2, and 0.1 mM of redox mediator (3,3',5,5'-tetramethylbenzidine,TMB; methylene blue, MB; hydroquinone, HQ), in the presence and absence of horse radish peroxidase (HRP). To study the dependence of the voltammetric response on the scan rate, [HRP] = 3 U×mL^{-1} was used, while varying the scan rate (5, 10, 20, 50, 100 mV×s^{-1}).

Chronoamperometric tests were performed after conditioning the CSPE with 3 CV Cycles in the pure PBS/KCl solution at 20 mV×s^{-1} from −0.30 V to 0.60 V. The e-ELISA was performed by transferring 100 μL of the solution contained in the wells onto the CSPE and performing a Chronoamperometry (CA) reading at a potential 100-150 mV lower than the reduction peak for 60 s. The calibration curves were obtained by plotting the current registered at 60 s, unless otherwise stated.

2.2. UV-visible measurements

The efficiency of cAb oxidation was evaluated via spectrophotometry. Oxidized cAb was prepared as described in Section 2.6, washed six times, and concentrated to 25× in 100 mM PBS. Untreated cAb was processed identically as a control. A 10 mg×mL^{-1} Purpald® solution in 1 M NaOH was prepared immediately before use. For the assay, 50 μL of each sample (oxidized cAb, unmodified cAb, or PBS blank) was added to 250 μL of Purpald® reagent (n = 3). Following a 90-min incubation, the mixtures were transferred to semi-micro cuvettes for UV-Vis spectral analysis. The transfer was performed just before the measurement to prevent the formation of bubbles inside the cuvette.

The stability of the redox mediators was evaluated over a period of 7 days by recording the absorption spectrum at wavelengths between 200 and 800 nm using a UV-visible (UV-vis) spectrophotometer. The mediator solutions were prepared at a concentration of 0.1 mM in 0.1 M PBS (pH 7), 0.1 M KCl, and stored in the refrigerator during the considered period. The TMB solution was prepared using an aqueous HCl solution at pH 5 and then diluted 1:3 in PBS at pH 7 for buffering. The measurements for the calibration curves of the commercial ELISA colorimetric kits were performed by transferring the solution from each well into cuvettes and diluting it to 300 μL with ultrapure water.

The BCA assay for evaluating the reproducibility of BSA coating on the wells was performed after coating with a 5.0 mg×mL^{-1} solution of denatured BSA in PBS, followed by the final three washing steps. Once the microplate was dried, 300 μL per well of freshly prepared BCA working reagent (prepared at a 20:1 ratio of Reagent A to Reagent B) was added. The plate was then incubated at 37 °C for 30 min and subsequently allowed to cool to room temperature for 15 min. Absorbance was then measured at 562 nm using a UV-Vis spectrophotometer.

2.3. H_2O_2 and TMB quantification

The H_2O_2 concentration of the commercial substrate solution was determined using the standard addition method, performing CA measurements on CSPEs. These responses were recorded at +0.05 V for 70 s in the presence of 3 U×mL^{-1} HRP, and considering the average current from 60 to 70 s as the analytical signal (Fig. S1).

The TMB concentration of the commercial substrate solution was determined directly from the electrochemical responses after calculating the calibration plot using TMB standard solutions and by sampling the anodic peak current in CV traces (Fig. S2). The CV responses were collected by scanning the potential from 0.00 to 0.60 V at 20 mV×s^{-1} in 0.1 M PBS (pH 7). Samples and standards were diluted 1:1 with a stop solution (1 M H_3PO_4, 0.1 M KCl). Based on these analyses, the measured concentrations of H_2O_2 and TMB were 1.2 mM and 1.5 mM, respectively.

2.4. Oriented covalent immobilization of cAb

The oriented covalent immobilization of the cAb on the uncoated polystyrene microplate required the prior oxidation of glycosyl residues on the cAb.

The following procedure was used to perform ELISA on 24 wells and achieve a final cAb concentration 5 times higher than the commercial kit. 28 μL of cAb were added to a vial containing a magnetic stir bar. PBS (10 mM, pH 7) was added to reach a total volume of 100 μL. Subsequently, 10 μL of 100 μM $NaIO_4$ was added, and the solution was incubated for 1 h in the dark under agitation. The content of the vial was quantitatively transferred to a 3 kDa centrifugal filter tube, washed three times with ultrapure water using a microcentrifuge. Finally, the oxidized cAb was resuspended in 2.8 mL of Coating Buffer (1×).

The cAb was then immobilized on sterile uncoated polystyrene microplates. A 5.0 $mg\times mL^{-1}$ BSA solution was prepared by dissolving the solid in 0.1 M PBS and denatured using a probe sonicator for 30 min with 1 s on/off intervals, for a total sonication time of 1 h. The coating solution was then prepared by adding GA to a final concentration of 1% in the denatured BSA/PBS solution (sufficient for a maximum of 8 wells per batch). Subsequently, 250 μL of the coating solution was poured into each well, and the microplate was incubated for 24 h at room temperature in a water-saturated atmosphere. Following the incubation, the microplate was washed three times with 0.1 M PBS (pH 7), with the second wash lasting longer than the standard ELISA procedure (10 min).

Afterwards, 100 μL/well of the oxidized cAb working solution previously described was added, and the plate was incubated overnight at 4 °C. The following day, a 0.2 mM NaOH solution containing 1 $mg\times mL^{-1}$ $NaBH_4$ was added (100 μL/well) and incubated for 30 min at room temperature. After removing the liquid, the plate was washed twice with wash buffer (0.05% Tween™-20, 0.137 M NaCl, 2.7 mM KCl, 10 mM Na_2HPO_4, and 1.8 mM KH_2PO_4).

2.5. Non-oriented covalent immobilization of cAb

The following procedure was used for the non-oriented covalent immobilization of the cAb on uncoated polystyrene microplates to generate a calibration curve in triplicate. Following the procedure described in Section 2.6 to coat the well with BSA, 100 μL/well of a freshly prepared solution containing EDC (400 mM) and NHS (200 mM) in 50 mM MES buffer were added. The microplate was then incubated in the dark for 30 min at room temperature to activate carboxyl groups for subsequent covalent immobilization of antibodies. After activation, the plate was washed three times with Milli-Q water, following the same timing as in the previous washing steps. Finally, after drying the microplate on absorbent paper, the cAb binding step was performed according to the procedure provided with the commercial ELISA kit. For the subsequent steps, follow the procedure described in Section 2.8.

2.6. e-ELISA procedure

The Human IL-18 Reference Standard (20000 pg) or the Human IgG Standard (1000 ng), previously reconstituted in 1 mL of 0.1% BSA, was thawed 10-30 min before use, and gently mixed. The standard was used immediately after reconstitution. An intermediate solution of 4000 $pg\times mL^{-1}$ IL-18 (or 200 $ng\times mL^{-1}$ IgG) was prepared by dilution with Milli-Q water. To generate the calibration curve, serial 1:1 dilutions of the standards were performed in triplicate by adding 100 μL/well of Assay Buffer A (1×). In the blank wells, 100 μL/well of Assay Buffer A (1×) and 100 μL of Milli-Q water were added. In the wells containing the real samples, 100 μL/well of Assay Buffer A (1×) and 100 μL of the sample, previously centrifuged at 10000 rpm for 20 min at 4 °C, were added. The plate was then covered and incubated at R.T. for 2 h. Following incubation, the liquid was removed, and four washes with Wash Buffer were performed.

The Detection Antibody (dAb) solution was prepared by diluting the biotinylated Human IL-18 (or Human IgG) dAb 1:500 in Biotinylated Antibody Diluent, and 100 μL/well were added to the plate. After covering, the plate was incubated at 37 °C for 1 h, followed by three washes. For each wash, the wells were aspirated and washed with 380 μL of Wash Buffer, with each wash lasting approximately 1 min. After washing, any residual buffer was removed by gently drying the microplate with absorbent paper. This is the general procedure for ELISA washing.

The HRP Conjugate working solution was then prepared by diluting the Human IL-18 (or Human IgG) HRP Conjugate 1:500 in HRP Conjugate Diluent, and 100 μL/well were added. The plate was incubated at 37 °C for 30 min, followed by five washes with Wash Buffer.

Fresh Substrate Solution (1.5 mM HQ, 1.2 mM H_2O_2 in 0.1 M PBS and 0.1 M KCl, pH 7) was added (100 μL/well), and the plate was incubated at room temperature for 30 min. At the end of the incubation, the solutions were transferred into clean wells, and the CA readout was performed as described in Section 2.3.

As a comparison, commercial ELISA colorimetric assays were performed according to the kit manuals.

2.7. 3D skin model

To obtain a 3D innervated artificial skin model, Scarpa et al. combined 3D printing based on MeHA for better reproducing dermis/epidermis and electrospinning based on PLLA for mimicking skin innervation as previously reported (Scarpa et al., 2026). Later, 3D artificial skin was colonized with a pre-neuronal cell line (SH-SY5Y), fibroblasts isolated from skin biopsies of an ALS Slow-progressing patient and a Fast-progressing patient, and healthy human dermal fibroblasts (HDF, controls, purchased from Sigma Aldrich, Milan, Italy). For fibroblast isolation, biopsies of the same 2 ALS patients used by Scarpa et al. (Scarpa et al., 2026), at different disease stages (Slow and Fast progressors) according to King's College staging system (Slow Progressor: Stage 2, patient characterized by involvement of a second anatomical region; Fast progressor: Stage 4A and 4B, patient with nutritional and respiratory failure, defined by the need for a feeding tube and non-invasive ventilation) were collected from patients recruited at the ALS center of Federico II University. Written informed consent was obtained from all subjects in accordance with the Declaration of Helsinki before enrollment in the study. The study protocol was approved by the local Ethics Committee (protocol number 100/17/ES01 and 151/2023), as reported in Scarpa et al. (Scarpa et al., 2026). Dermal fibroblasts were isolated from skin biopsies by using the protocol described by Iannello et al. (2023). After cell isolation, 3D artificial skin was colonized with SH-SY5Y and fibroblasts (HDF, Slow and Fast). In detail, for each 3D structure, SH-SY5Y cells (2×10^4) were seeded on electrospun PLLA surface for mimicking skin innervation, meanwhile fibroblasts (2×10^4) isolated from skin biopsy of ALS patients at different disease stages (Slow and Fast) or HDF cells as healthy control, were seeded on 3D printed MeHA for better reproducing dermis/epidermis. After 7 days of cell co-culture, ISF was extracted from 3D skin model through needle sampling and centrifuged for 20 min at 10000 rpm at 4 °C to remove any cellular contaminants and debris.

To characterize 3D skin model's morphology, the analysis was performed by Scanning Electron Microscopy (SEM; FEI Quanta 200 FEG, Eindhoven, The Netherlands) on the PLLA/MEHA skin model. To this aim, after sample fabrication and freeze-drying, samples were coated with an ultrathin layer of Au/Pt by using an ion sputter.

For the analysis of cell morphology, each cell line was grown for 7 days (2×10^4 cells for each cell line) onto the 3D structure. After this time, samples were fixed with a solution of 4% w/v paraformaldehyde (PFA) overnight at 4 °C. Then, samples were washed thrice with PBS 1× and permeabilized in 0.1% v/v BSA +0.03% v/v Triton-100X solution for 1 h. Later, samples were washed thrice with PBS 1X and stained with anti-Phalloidin-ATTO 594 (Molecular Probes®, Life Technologies) solution (1:200) for 1 h. Later, samples were washed, and nuclei were counterstained with 10 $\mu g\times mL^{-1}$ DAPI. Finally, samples were washed with PBS 1× thrice, and cell images were acquired with a fluorescence microscope at magnification 10× (Leica DMi8 microscopes).

3. Results and discussion

3.1. The cAb immobilization strategy

Several parameters must be optimized during the development of an e-ELISA to achieve the technique's full potential. Among these parameters, we first investigated the effect of different immobilization methods for the cAb on the well plate surface. We compared two covalent strategies, one with random orientation and another with controlled orientation, to the most common, non-covalent binding strategy used in commercial *high-binding* plates. These commercial plates are optimized for high binding capacity via a combination of hydrophobic and ionic interactions. Unfortunately, they have proprietary compositions, making it difficult to translate the ELISA technology to an electrochemical reading, for which a versatile anchoring strategy of the primary antibody is crucial.

To overcome these limitations, we developed two covalent anchoring strategies inspired by recent work from Ingber and colleagues (Sabaté del Río et al., 2019; Timilsina et al., 2022). The methods involve creating a thin film of cross-linked, denatured BSA on the well's surface using a 1% final concentration of GA (Fig. 1A). BSA was denatured by ultrasonication with a tip sonicator. The BSA film serves a dual purpose: it acts as a coating to prevent non-specific binding and provides a high density of amine and carboxylic groups for cAb immobilization.

For the random immobilization strategy, we formed a chemical bond between the antibody's amine groups and the carboxylic groups of the denatured BSA film, creating a stable amide bond (Fig. 1A), after activation of the carboxylic acid with EDC and NHS. Since amine groups are distributed throughout the antibody's structure (on both heavy and light chains), this method results in a random orientation of the cAb. A potential drawback is that the epitope may be unintentionally oriented toward the well's surface, making it unavailable to bind to the target analyte.

To ensure proper cAb orientation, we exploited the glycosidic moieties found primarily on the antibody's heavy chain (Fig. 1A). (Batalla et al., 2008; Sharma et al., 2016) For this purpose, the hydroxyl groups of these carbohydrates were oxidized to form aldehydes using $NaIO_4$. The efficiency of the cAb oxidation has been evaluated using a spectrophotometric assay using Purpald® to react selectively with aldehyde residues (Jeevarathinam et al., 2025; Lee and Tsai, 1999). The results indicate the successful oxidation, assessed by a more than 3-fold increase in the absorbance at 550 nm compared to the unmodified cAb (Fig. S3). The formed aldehydes then reacted with the amine groups of the denatured BSA, forming imine bonds and ensuring that the antibody's antigen-binding sites were consistently facing outward and available to interact with the analyte. Finally, the imine bond was reduced to an amine, using $NaBH_4$, to improve the stability of the functionalization.

In the first instance, we performed ELISA tests using h*igh-binding* plates (non-covalent immobilization) and a commercial substrate solution containing TMB and H_2O_2, which allowed contemporaneous HRP-mediated colorimetric (absorbance at 450 nm, Fig. S4) and amperometric readout (Fig. 1B; Fig. S5A).

The CA measurements were recorded by dropping the solution on a CSPE over 60 s at an applied potential of +0.2 V. This potential was selected based on the electrochemical response recorded on this electrode surface (Fig. S5B), to ensure that TMB reduction occurs in diffusion-limited conditions to achieve the highest sensitivity and reproducibility.

The calibration curves obtained from the electrochemical readout for the different immobilization strategies (non-covalent interaction, random covalent bonds, and oriented covalent bonds) are shown in Fig. 1B, C, and 1D, respectively. The data points represent the current sampled after 5 s of polarization at the fixed potential chosen. A comparison of the electrochemical (Fig. 1B) and optical readouts (Fig. S4B) from the *high-binding* plates revealed similar trends, confirming the viability of the electrochemical method and the appropriateness of the chosen experimental conditions.

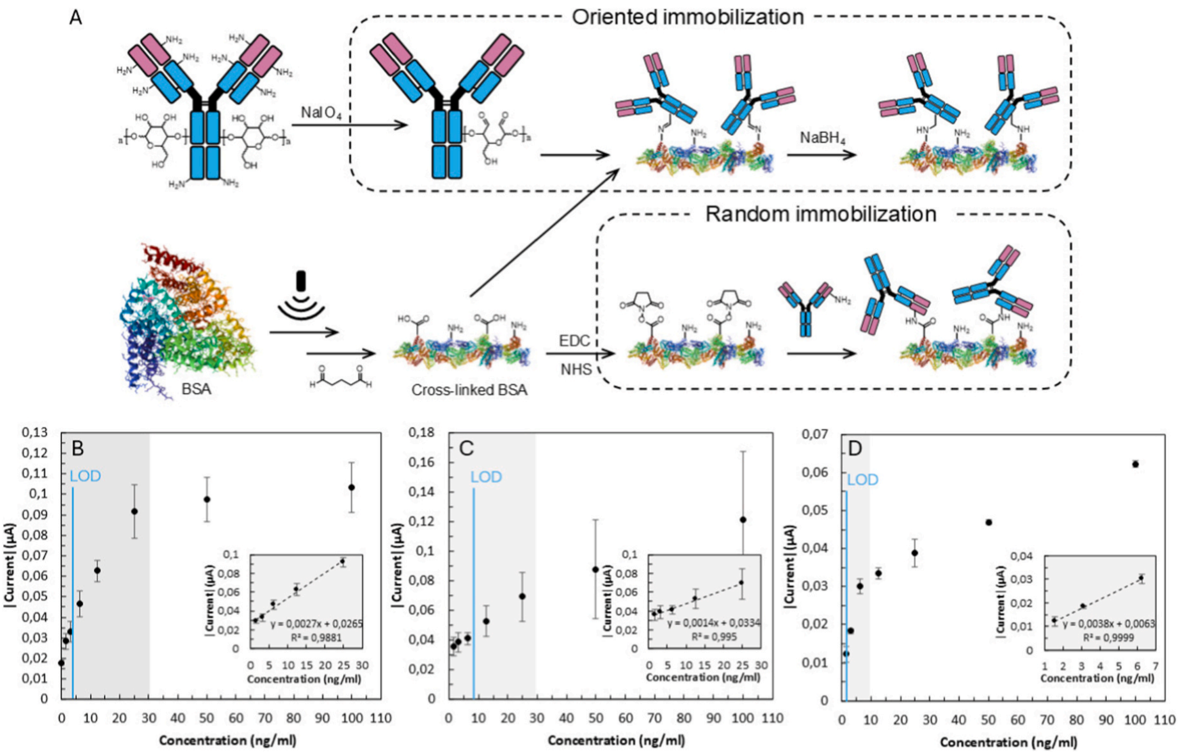

Fig. 1. The impact of the functionalization strategy. A) Scheme representing the oriented and random covalent immobilization strategies. Calibration line for IgG obtained by CA readout (E = +0.20V) with TMB substrate solution using high-binding plates (B), random covalent immobilization strategy (C), and oriented covalent immobilization strategy (D). Data represent mean ± SD (n = 3).

Comparing the three immobilization approaches tested, we could observe that the random covalent method yielded lower sensitivity and higher limits of detection (LODs) (Table S1). This is likely because the *high-binding* plates are optimized to immobilize a high density of proteins, whereas the receptor density achieved with our random covalent method was lower under the tested conditions. However, the oriented immobilization dramatically increased sensitivity to 0.016 μA×ng×mL^{-1}×cm^{-2} (Table S1). Notably, the LOD was 1.91 ng×mL$^{-1,}$ which is even lower than that obtained with the commercial *high−binding* plates. These results align with findings from Lozano−Chamizo et al., who demonstrated that oriented antibody immobilization can reduce the LOD and increase sensitivity in graphene field effect transistors (Lozano-Chamizo et al., 2024). The improved performance is attributed to the correct orientation of the antibody epitopes, which facilitates antigen binding and enables the detection of lower analyte concentrations. As Tajima et al. have shown, well-oriented antibodies can form antigen-antibody complexes up to 100 times stronger, significantly enhancing binding affinity (Tajima et al., 2011). A limitation of the oriented covalent immobilization method is the reduced linear range (1.56 to 6.25 ng×mL^{-1}). This may be because the lower number of cAb anchored via covalent immobilization leads to a rapid saturation of the available binding sites.

3.2. *The choice of the best electrochemical mediator*

The electrochemical mediator is a core element of e-ELISA, transferring electrons between the enzyme and the electrode to generate the electrical signal. Researchers have explored various redox mediators for

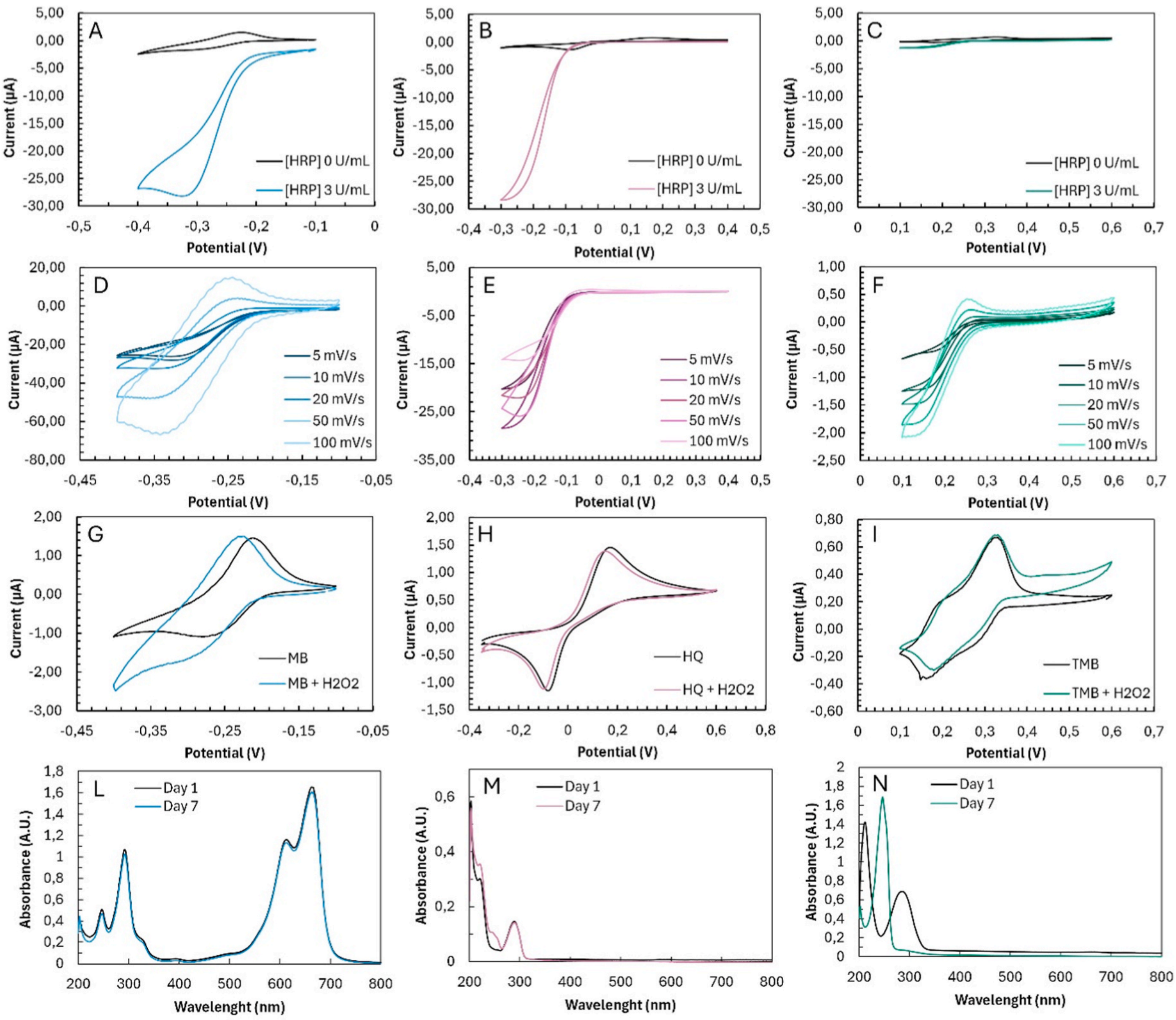

P	Generated Current	Operational Stability	Storage Stability
	i_{pc} (μA)	$\frac{(i_{pc(Cycle1)}-i_{pc(Cycle4)})}{i_{pa(Cycle1)}} * 100$ (%)	$\frac{(i_{pc(Day1)}-i_{pc(Day6)})}{i_{pc(Day1)}} * 100$ (%)
MB	-28.16	-28.60	-3.12
HQ	-27.96	-14.47	-23.28
TMB	-1.21	-63.34	-65.63

Fig. 2. The impact of the best electrochemical mediator. CV responses of 0.1 mM MB (A), HQ (B), and TMB (C) and 2 mM H_2O_2 (2 mM), in the absence and in the presence of 3 U×mL^{-1} HRP. The analysis was performed in 0.1M PBS (pH 7.0) with 0.1M KCl at a scan rate of 0.01 V×s^{-1}. CV responses of 0.1 mM MB (D), HQ (E), and TMB (F), 2 mM H_2O_2 (2 mM), and 3 U×mL^{-1} HRP at different scan rates. CV responses of 0.1 mM MB (G), HQ (H), and TMB (I) in the absence and in the presence of 2 mM H_2O_2. UV-visible spectra of MB (L), HQ (M), and TMB (N) solutions were collected just after preparation and after 7 days. P) Table resuming the current generated by electrochemical reduction of the redox mediator (0.1 mM) in 2 mM H_2O_2 solutions after the addition 3 U×mL^{-1} HRP, the operational stability (defined as the percentual change of the cathodic current after 4 CV cycles), and the storage stability (defined as the percentual variation of the cathodic current after 6 days of storage of the mediator solution).

HRP-based e-ELISA (e.g., TMB (Höfs et al., 2021), HQ (Manoj et al., 2022; Martins et al., 2021; Valverde et al., 2020), MB (Álvarez-Martos et al., 2017), catechol (Serafín et al., 2011), methylene green (Upadhyay et al., 2009b), nile blue (Upadhyay et al., 2009a), thionine (Monisha et al., 2025), toluidine blue (Thenmozhi and Narayanan, 2017), ferrocene (Chen et al., 2024) and its derivatives (Tian et al., 2024)) but a direct comparison of the electrochemical mediator efficiency is still missing. Among these, TMB is the most widely used substrate for HRP-based ELISA due to its high molar absorbance in visible spectroscopy. Due to its popularity in colorimetric ELISA and the numerous commercial TMB-based solutions, this substrate became a popular choice for e-ELISA-based immunosensors. But is it the best electrochemical mediator we can use?

To answer this question, we performed a comparative study between three of the most common electrochemical mediators for HRP: TMB, MB, and HQ. We evaluated the main aspects that can affect the analytical performance of e-ELISA tests, such as sensitivity, background current, and LODs. The parameters considered were: 1) the current generated by the HRP-catalyzed electrochemical cycle; 2) the kinetics of the enzymatic reaction; 3) the background current resulting from the direct oxidation of the mediator by H_2O_2; 4) the stability of the mediator during the electrochemical measurement; 5) the shelf-life of the mediator during storage.

Fig. 2A, B, and C report the CV responses recorded in the absence and in the presence of HRP for MB, HQ, and TMB, respectively. All the voltammograms were registered in the presence of 0.1 mM of the mediator and 2 mM of H_2O_2 with a scan rate of 10 $mV \times s^{-1}$.

In the presence of HRP, redox mediators exhibit typical electrocatalytic voltammetric responses. The catalytic cycle (Scheme 1) begins when H_2O_2 oxidizes native ferric HRP (Fe^{III}) into a reactive π-cation radical intermediate (E_1). This intermediate is then reduced back to the Fe^{III} state through two sequential one-electron transfers from the reduced mediator M_{red}, passing through an oxyferryl intermediate (E_2). This cycle consumes one H_2O_2 and two M_{red} molecules to produce two oxidized mediators M_{ox} (Dequaire et al., 2002).

Generating an electrocatalytic cycle between HRP and the electrode surface is a crucial strategy for signal amplification in sandwich e-ELISAs. By boosting the electrochemical response, this mechanism enhances immunosensor sensitivity and analytical performance, enabling the detection of analytes at significantly lower concentrations.

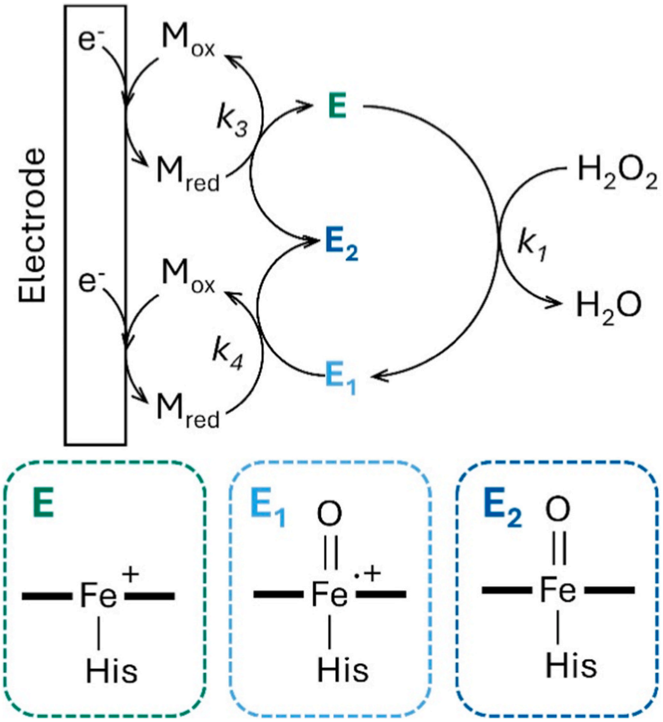

Scheme 1. The catalytic cycle of HRP.

As shown in Fig. 2A, B, C, the M_{ox} generated by the enzyme is rapidly reduced on the electrode surface, producing a much higher signal when HQ and MB are used. The resulting cathodic current is more than 20 times higher than that observed when TMB is used. The current enhancement directly translates into higher sensitivity, making HQ and MB better choices for e-ELISA and immunosensor applications.

The electrochemical signal varies significantly with reaction conditions. Under limiting conditions (e.g., low H_2O_2 or high scan rates), the response is diffusion-controlled and provides no further information. Conversely, under ideal conditions (e.g., high H_2O_2 or low scan rates), the voltammogram adopts a characteristic S-shaped plateau proportional to HRP and H_2O_2 concentrations. (Dequaire et al., 2002).

As shown in Fig. 2D–F, varying the scan rate reveals the kinetic differences between the tested mediators. HQ maintains the characteristic S-shaped catalytic curve even at high scan rates 0.1 $V \times s^{-1}$, whereas MB and TMB lose this signature at much lower rates (0.02 $mV \times s^{-1}$ and 0,005 $mV \times s^{-1}$, respectively). These data confirm that the kinetics of enzymatic mediator oxidation follow the order: HQ > MB > TMB.

Another factor to consider is whether the electrochemical mediator is directly oxidized by H_2O_2 in the absence of the HRP. Indeed, this side pathway can generate a background current that is independent of the enzyme concentration, reducing the signal-to-noise ratio and affecting the LODs. Of the three tested mediators, HQ proved to be the least affected by the presence of H_2O_2. (Fig. 2G, H, I).

The stability of the three mediators was evaluated in terms of both operational and storage performance. The stability of the voltametric response was assessed by monitoring the change in the cathodic peak current over four consecutive CV scans, as detailed in Fig. S6. The results, presented in Fig. 2P as the percentage variation between the first and fourth CV, demonstrate that HQ exhibits the most stable response during electrochemical measurements. This is followed by MB and TMB, with the latter showing a massive signal decrease.

For shelf life, the cathodic current was measured after storing the mediator solutions at 4 °C for 1, 3, and 6 days (Fig. S7). MB demonstrated the best shelf-life, with only a 3.14% reduction in signal after six days. This was significantly better than HQ, which saw a 23.28% reduction, and TMB, with a substantial 65.63% drop.

To understand these variations, UV-Vis spectra were collected over time, namely, soon after the preparation and after 7 days. MB's spectrum remained constant, indicating excellent stability within the tested timelapse (Fig. 2L). HQ's poor stability was attributed to partial oxidation to benzoquinone (BQ), which was confirmed by the appearance of a new peak at 245 nm (Fig. 2M) (Samiee et al., 2016). Finally, the spectra collected for TMB evidence the disappearance of peaks at 211 and 286 nm and the arising of a new peak at 247 nm (Fig. 2N). This significant variation of the solution composition supports the dramatic variation of the electrochemical signal recorded for TMB over time.

An advantage of HQ over MB is its less negative reduction potential, which prevents it from overlapping with the direct reduction of H_2O_2 or oxygen, which may affect the accuracy of the amperometric detection.

In conclusion, under the conditions tested in this work, HQ proved to be the best electrochemical mediator and was therefore selected for the development of the e-ELISAs for Human IgG and IL-18. To obviate the limited shelf life of HQ, we used freshly prepared solutions for all experiments.

It is important to note that these findings are specific to CSPE and may not apply to other electrode surfaces. For example, HQ on gold electrodes is subject to high overpotentials, which render the redox reaction quasi-irreversible and thus less suitable for use in immunosensors or e-ELISA.

3.3. *The optimization of the operational parameters for the detection of Human IgG*

Optimization of the Human IgG e-ELISA began with quantifying TMB and H_2O_2 in commercial substrates to establish reference values. The H_2O_2 concentration was determined via the standard addition method (Fig. S1) while TMB levels were derived directly from its electrochemical response (Fig. S2).

Building on these reference values, we optimized the concentrations of the cAb, of H_2O_2, and of HQ to maximize the CA signal for our e-ELISA based on the oriented covalent immobilization. cAb was tested at concentration levels 1×, 3×, and 5× compared to the commercial kit's recommendation, HQ at concentrations of 0.5 mM, 1.5 mM, and 2.5 mM, and H_2O_2 at concentrations equal to 0.4 mM, 1.2 mM, and 2.0 mM. Our goal was to identify the concentration of reagents that produced the highest net current (measured by CA), which was calculated as the difference between the signal from a 25 ng×mL^{1} antigen sample and the blank, without losing reproducibility (Fig. 3 A, B, C). The conditions providing the maximum CA signal were 5× cAb, 1.5 mM HQ, and 1.2 mM H_2O_2 in a solution of 0.1 M PBS (pH 7) and o.1 mM KCl (HQ Substrate Solution).

Standard stop solutions (e.g., 1 M H_3PO_4) failed to halt the HRP/HQ reaction. While acid stops the process by protonating TMB, it does not similarly inhibit HQ. Moreover, even at this suboptimal pH the enzyme retains sufficient activity to continue the catalytic cycle (Fong and Cruess, 1929; Tabatabaei and Ahmed, 2022). To ensure accurate, time-fixed measurements, we implemented a physical separation by transferring the reaction supernatant to clean wells, effectively terminating the enzymatic reaction.

The reproducibility and repeatability of the well coating were optimized by using freshly prepared BSA solutions and increasing the coating volume from 100 to 250 μL. To ensure consistent cross-linking and minimize premature aggregation, a BSA-GA solution was prepared in small aliquots (sufficient for a maximum of eight wells at a time) and applied rapidly. The coating's reproducibility was confirmed by a bicinchoninic acid (BCA) assay, which yielded a relative standard deviation (RSD) of 6.5% across the wells (Fig. S8).

To optimize the assay's sensitivity, we investigated the effect of substrate incubation time on the electrochemical signal (Fig. 3D). The net current was calculated as the difference between the signal from a 25 ng×mL^{-1} antigen solution and the blank. We tested various incubation times (5, 10, 15, 30, and 60 min) for the HQ-Substrate Solution. An incubation time of 30 min was selected as an optimal compromise between achieving high sensitivity and maintaining reasonable operational times.

Finally, under the optimized conditions, the calibration curve for Human IgG detection was constructed using CA measurements, applying a potential of −0.2 V for 60 s and covering concentrations from 0 to 100 ng×mL^{-1}. (Fig. 3E and F). The comparison with the preliminary curve obtained before optimization (Fig. 1D) revealed a significant improvement in the sensitivity (0.025 μA×ng^{-1}×mL×cm^{-2}) and in the linear range, extended to the entire set of explored concentrations. The LOD found in these optimized conditions (5.12 ng×mL^{-1}) is useful for the determination of the antigen in biological fluids (e.g., blood, saliva, and breast milk). These results confirm the effectiveness of the parameter optimization and the robustness of the developed e-ELISA for Human IgG detection.

3.4. *Quantification of IL-18 in 3D skin models from ALS patients*

Finally, we applied the optimized e-ELISA protocol to 3D skin models, developed by Fasolino and coworkers (Scarpa et al., 2026) to test the ability of the developed assay to discriminate between cell cultures obtained by ALS patients with different disease progression. The 3D model is schematically reported in Fig. 4A, together with SEM micrographs showing the morphological features of the model. Specifically, the region devoted to skin innervation results in micrometric oriented PLLA fibers, meanwhile the one recapitulating the dermis/epidermis by a morphologically controlled MeHA-based structure. The scaffold's architecture ensures high structural stability and porosity suitable for cell colonization, with mechanical properties matching native skin (Scarpa et al., 2026). Furthermore, biological validation confirmed the model's biocompatibility, promoting the survival of each cell line over 7 days of culture (Scarpa et al., 2026). In Fig. 4B shows the morphological features of each fibroblast cell line [CTRL (HDF), Slow, and Fast ALS fibroblasts) at the interface with neuronal cells, mimicking innervation. The images revealed that the 3D skin model allows reproducing innervated skin and promotes the interaction between several cell phenotypes that colonize skin biopsies. Qualitative results confirmed differences in cell morphology of healthy (HDF) and ALS

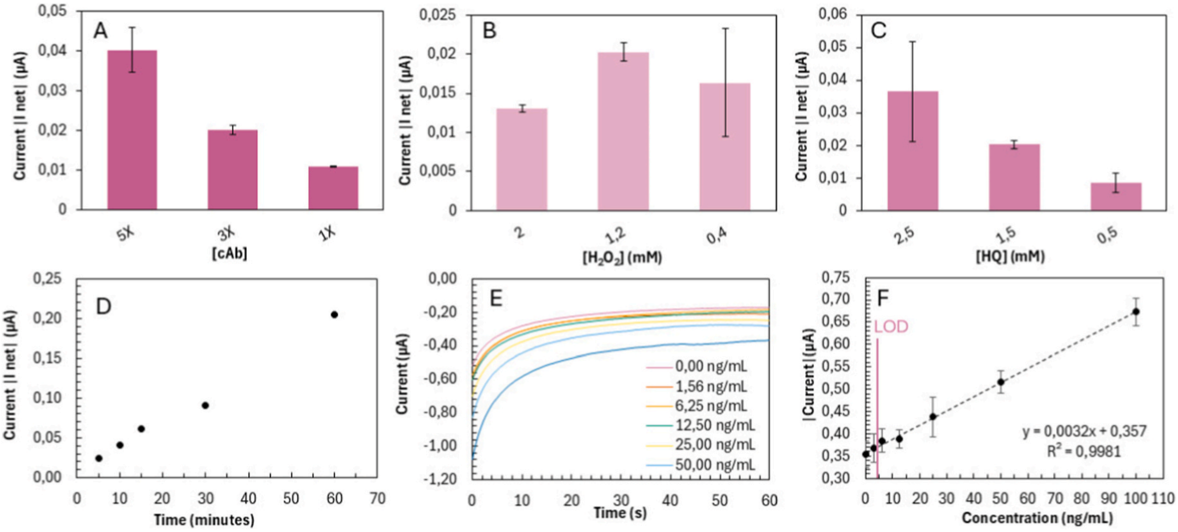

Fig. 3. The optimization of the operational parameters for the detection of IgG. A) Net current registered for the e-ELISA test in the presence of 25 ng×mL^{-1} IgG at different concentrations of cAb. B) Net current registered for the e-ELISA in the presence of 25 ng×mL^{-1} IgG at different concentrations of H_2O_2. C) Net current registered for the e-ELISA in the presence of 25 ng×mL^{-1} IgG at different concentrations of HQ. D) Optimization of the incubation time with the HQ Substrate Solution. (n = 1) E) CA response of the e-ELISA F) Calibration line obtained for IgG using the optimal conditions identified in this work. Data represent mean ± SD (n = 3).

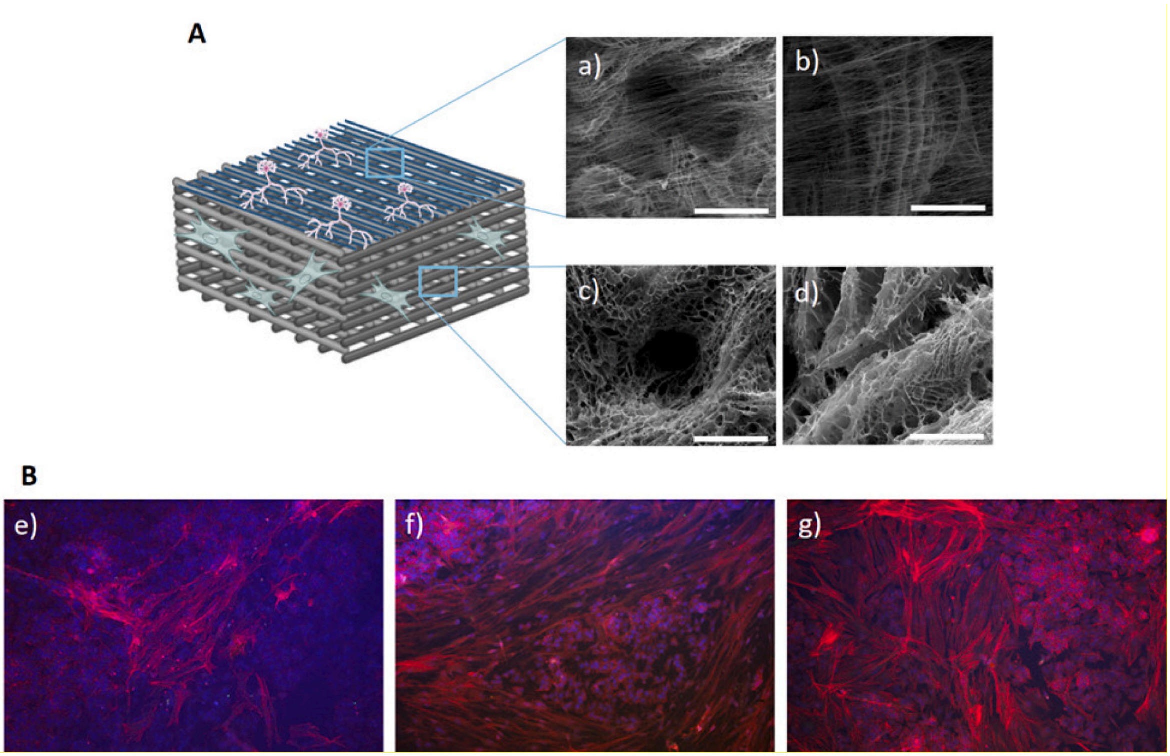

Fig. 4. A) Schematic representation of the 3D skin tissue model obtained by combining electrospinning and 3D printing and SEM images of the different regions where it is well visible the electrospun layer (a-b) on the 3D printed one (c-d). Scale Bars: 1 mm (a-c) and 500 μm (b-d). B) Morphological features of each fibroblast cell line [HDF, (e), Slow,(f) and Fast, (g) ALS fibroblasts] grown on 3D skin model at the interface with neuronal (SH-SY5Y) cells. The images are representative of 3 independent experiments. Magnification: 10 × . Scale bar: 100 μm.

fibroblasts, thus making the 3D skin model an efficient tool to screen ALS pathology because it doesn't change biological response. Indeed, Fig. 4B showed that HDF stored the expected normal spindle-shaped morphology after 7 days of cell culture. Meanwhile, Slow and Fast ALS fibroblasts displayed enlarged bodies and nucleoli as a result of inflamed conditions (Scarpa et al., 2026). The 3D skin model, using patient-derived cells, confirmed the link between ALS neurodegeneration and the inflammasome cascade activation. Analysis revealed that p-TDP43 accumulation correlates with the activation of the pyroptosis cascade, evidenced by elevated levels of NLRP-3, IL-18, IL-6, and nitrites (Scarpa et al., 2026). For this reason, this 3D artificial skin constitutes a valid tool for identifying, in a more accurate model that approximates in vivo conditions (skin biopsy samples), novel ALS biomarkers useful to have information on ALS disease etiology, severity and progression.

To quantify IL-18 levels in the 3D skin models, we generated calibration lines in triplicate using IL-18 standards. The data show a logarithmic dependency of the current on IL-18 concentration, as measured by CA at 60 s (Fig. 5A–B). The values of LOD and LOQ were calculated to be 1.77 pg×mL^{-1} and 6.70 pg×mL^{-1}, respectively, which are significant for IL-18 detection in real samples.

The quantification of IL-18 in the ISF, extracted from Fast (246.95 ± 97.93 pg×mL^{-1}) and Slow-progressing (122.75 ± 8,62 pg×mL^{-1}) ALS models, evaluated in triplicate, revealed significantly higher levels compared to the healthy control model (73,88 ± 13,06 pg×mL^{-1}) (Fig. 5C). This marks a crucial leap forward in diagnosis, confirming IL-18's utility as a robust ALS detection biomarker. The consistent signals, which were well above the LOQ, further attest to the exceptional quantitative capability of the e-ELISA platform across all models. The most significant finding, however, lies in the differentiation of disease severity: the Fast-progressing ALS model exhibited a significantly higher IL-18 concentration than the Slow-progressing model. This is a critical advance compared to the commercial ELISA kit, which could not distinguish differences in IL-18 levels of Fast and Slow ALS progressors (Scarpa et al., 2026). Thus, by utilizing fibroblasts isolated from Fast and Slow-progressing patients within a 3D skin model, we could establish a platform capable of mirroring patient-specific disease severity. IL-18 was selected as the biosensor

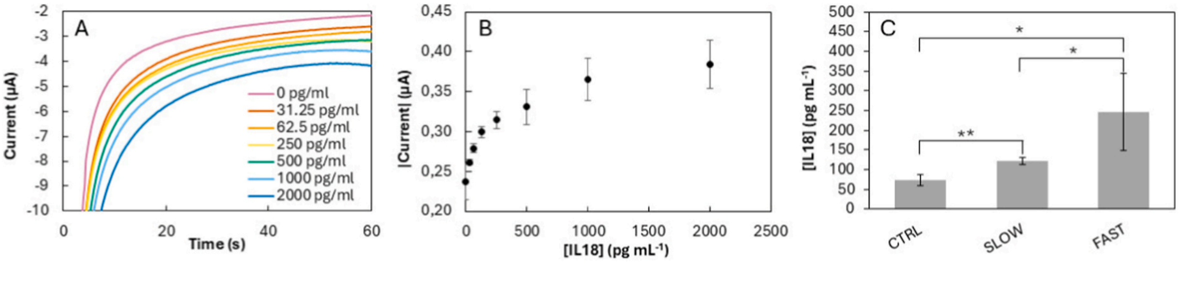

Fig. 5. e-ELISA protocol applied to the detection of IL-18 in the ISF obtained by 3D skin models derived from ALS patients. A) CA responses registered in 0.1M PBS 0.1M KCl at different IL-18 concentrations ([IL-18] = 0, 31.3, 62.5, 125, 250, 500, 1000, 2000 pg×mL^{-1}) at a potential of −0.2 V. B) Calibration curve for IL-18. C) concentration of IL-18 obtained from the e-ELISA assay applied to the ISF of 3D skin models. Data represent mean ± SD (n = 3). *$p \leq 0.05$, **$p \leq 0.01$.

target due to its primary role in the inflammasome cascade. Biochemical data (Scarpa et al., 2026) show that IL-18 is released more significantly than IL-6 and correlates closely with NLRP-3 and p-TDP43 expression in a 3D skin model. As p-TDP43 scales with disease severity, IL-18 serves as a key effector driving the chronic neuroinflammation that sustains ALS progression.

This result addresses a major unmet need in the ALS field, as it provides preliminary evidence that IL-18 levels, as measured by e-ELISA, may have the potential to differentiate between Fast- and Slow-progressing ALS phenotypes. However, further validation in larger clinical cohorts is required to establish definitive diagnostic cutoff values. This work offers a pathway toward a less invasive and more timely diagnosis, paving the way for personalized treatment strategies tailored to individual disease severity.

4. Conclusions

We developed a highly optimized e-ELISA for the sensitive quantification of IL-18, identifying it as a potential ALS biomarker. The high performance of the developed method was achieved through systematic technical advances with respect to conventional ELISA. A key finding was the use of a BSA-crosslinked coating, which simultaneously ensured the oriented covalent immobilization of antibodies and effectively prevented non-specific binding, thereby significantly lowering the LOD. Furthermore, adopting HQ as the electrochemical mediator yielded rapid HRP enzymatic kinetics and intense current signals, which further enhanced overall assay sensitivity. Despite its superior performance, HQ's limited stability in solution may affect its commercial viability. To mitigate this, HQ could be formulated as pre-dosed tablets or pellets, similar to standard ELISA kits, allowing for fresh dissolution immediately before use and bypassing storage-related degradation.

Using a 3D innervated skin model, we demonstrated that e-ELISA can distinguish between a Fast- and a Slow-progressing ALS model, based on IL-18 expression in the ISF. While this confirms the technology's potential for personalized monitoring, large-scale validation is required to establish standardized clinical diagnostic thresholds for IL-18.

Our systematic optimization provides a versatile framework for developing high-performance sensors targeting broader neuroinflammation panels. This e-ELISA chemistry is ideal for integration into portable, microfluidic point-of-care devices, enabling automated ISF sampling, washing, and multiplexed detection. Ultimately, this method paves the way for rapid, personalized tools to enhance clinical management of neurodegenerative diseases.

Declaration of generative AI and AI-assisted technologies in the manuscript preparation process

The authors used AI (Gemini) to improve the manuscript's readability and language. After using this tool, the authors carefully reviewed and edited the content as needed and took full responsibility for the publication's content. All images in this work were created using licensed graphic software without artificial intelligence.

Funding sources

The authors acknowledge support from “Progetti di Ricerca di Rilevante Interesse Nazionale (PRIN)” Next Generation EU MUR, Rif. Bando PRIN 2022 PNRR- SENSATI-ON-ALS, Grant No. P20229JNTM.

CRediT authorship contribution statement

Nicola Furlan: Formal analysis, Investigation, Methodology, Writing – original draft, Writing – review & editing. **Ugo D'Amora:** Conceptualization, Investigation, Methodology, Writing – original draft, Writing – review & editing. **Ines Fasolino:** Conceptualization, Funding acquisition, Investigation, Methodology, Project administration, Writing – original draft, Writing – review & editing. **Alessandro Silvestri:** Conceptualization, Data curation, Formal analysis, Investigation, Methodology, Project administration, Supervision, Writing – original draft, Writing – review & editing. **Chiara Zanardi:** Conceptualization, Project administration, Supervision, Writing – review & editing.

Declaration of competing interest

The authors declare that they have no known competing financial interests or personal relationships that could have appeared to influence the work reported in this paper.

Acknowledgements

The authors acknowledge Prof. Raffaele Dubbioso for providing skin biopsies for the fibroblast isolation.

Appendix A. Supplementary data

Supplementary data to this article can be found online at https://doi.org/10.1016/j.bios.2026.118567.

Data availability

Data for this article are available at the Datarepository Unive (https://datarepository.unive.it/) The data are identified by the following DOI: https://doi.org/10.71731/DATA_UNIVE/97YASN to facilitate their findability.

References

Arya, S.K., Estrela, P., 2018. Biosens. Bioelectron. 117, 620–627. https://doi.org/10.1016/j.bios.2018.07.003.

Arya, S.K., Estrela, P., 2020. Sensors 20. https://doi.org/10.3390/s20102857.

Batalla, P., Fuentes, M., Grazu, V., Mateo, C., Fernandez-Lafuente, R., Guisan, J.M., 2008. Biomacromolecules 9, 719–723. https://doi.org/10.1021/bm7010906.

Chen, C.-Y., Motabar, D., Zakaria, F.R., Kim, E., Wu, B., Payne, G.F., Bentley, W.E., 2024. Biotechnol. Bioeng. 121, 3754–3767. https://doi.org/10.1002/bit.28839.

Deora, V., Lee, J.D., Albornoz, E.A., McAlary, L., Jagaraj, C.J., Robertson, A.A.B., Atkin, J.D., Cooper, M.A., Schroder, K., Yerbury, J.J., Gordon, R., Woodruff, T.M., 2020. Glia 68, 407–421. https://doi.org/10.1002/glia.23728.

Dequaire, M., Limoges, B., Moiroux, J., Savéant, J.-M., 2002. J. Am. Chem. Soc. 124, 240–253. https://doi.org/10.1021/ja0170706.

Downer, M.B., Li, L., Carter, S., Beebe, S., Rothwell, P.M., 2023. Neurology 101, e645–e652. https://doi.org/10.1212/WNL.0000000000207479.

Fong, W.Y., Cruess, W.V., 1929. Plant Physiol. 4, 537–541. https://doi.org/10.1104/pp.4.4.537.

Höfs, S., Hülagü, D., Bennet, F., Carl, P., Flemig, S., Schmid, T., Schenk, J.A., Hodoroaba, V., Schneider, R.J., 2021. Chemelectrochem 8, 2597–2606. https://doi.org/10.1002/celc.202100446.

Iannello, G., Patel, A., Sirabella, D., Diaz, A.G., Hoover, B.N., Sarmah, H., Corneo, B., 2023. Curr. Protoc. 3, e714. https://doi.org/10.1002/cpz1.714.

Irwin, K.E., Sheth, U., Wong, P.C., Gendron, T.F., 2024. Mol. Neurodegener. 19, 9. https://doi.org/10.1186/s13024-023-00685-6.

Jeevarathinam, A.S., Kawelah, M.R., Han, S., Grindel, B.J., Millward, S.W., Johnston, K. P., Sokolov, K.V., 2025. Nat. Protoc. 1–28. https://doi.org/10.1038/s41596-025-01272-3.

Lee, C.-H., Tsai, C.-M., 1999. Anal. Biochem. 267, 161–168. https://doi.org/10.1006/abio.1998.2961.

Lozano-Chamizo, L., Márquez, C., Marciello, M., Galdon, J.C., de la Fuente-Zapico, E., Martinez-Mazón, P., Gonzalez-Rumayor, V., Filice, M., Gamiz, F., 2024. Biosens. Bioelectron. 250, 116040. https://doi.org/10.1016/j.bios.2024.116040.

Álvarez-Martos, I., Shahdost-fard, F., Ferapontova, E.E., 2017. Electrochim. Acta 249, 206–215. https://doi.org/10.1016/j.electacta.2017.07.161.

Manoj, D., Rajendran, S., Gracia, F., Ansar, S., Santhamoorthy, M., Soto-Moscoso, M., Gracia-Pinilla, M.A., 2022. Environ. Res. 215, 114427. https://doi.org/10.1016/j.envres.2022.114427.

Martins, T.S., Bott-Neto, J.L., Oliveira, O.N., Machado, S.A.S., 2021. Microchim. Acta 189, 38. https://doi.org/10.1007/s00604-021-05145-w.

Milne, S.A., Lasserre, P., Corrigan, D.K., 2024. Analyst 149, 4736–4746. https://doi.org/10.1039/D4AN00392F.

Monisha, S., Sain, A., Jayaprakash, N.S., Senthil Kumar, A., 2025. Facile antibody. Langmuir 41, 4446–4456. https://doi.org/10.1021/acs.langmuir.4c03620.

Nolano, M., Provitera, V., Caporaso, G., Fasolino, I., Borreca, I., Stancanelli, A., Iuzzolino, V.V., Senerchia, G., Vitale, F., Tozza, S., Ruggiero, L., Iodice, R., Ferrari, S., Santoro, L., Manganelli, F., Dubbioso, R., 2024. Brain J. Neurol. 147, 1740–1750. https://doi.org/10.1093/brain/awad426.

Sabaté del Río, J., Henry, O.Y.F., Jolly, P., Ingber, D.E., 2019. Nat. Nanotechnol. 14, 1143–1149. https://doi.org/10.1038/s41565-019-0566-z.

Sajeevan, A., Sukumaran, R.A., Panicker, L.R., Kotagiri, Y.G., 2025. Microchim. Acta 192, 80. https://doi.org/10.1007/s00604-024-06916-x.

Samiee, F., Pedron, F.N., Estrin, D.A., Trevani, L., 2016. J. Phys. Chem. B 120, 10547–10552. https://doi.org/10.1021/acs.jpcb.6b07893.

Scarpa, E., D'Amora, U., De Cesare, N., Bonadies, I., Dubbioso, R., Nolano, M., Dardano, P., De Stefano, L., Fasolino, A., Zeppetelli, S., Silvestri, A., Zanardi, C., Milella, E., Fasolino, I. ACS Appl. Mater. Interfaces 2026. https://doi.org/10.1021/acsami.5c23366.

Serafín, V., Eguílaz, M., Agüí, L., Yáñez-Sedeño, P., Pingarrón, J.M., 2011. Electroanalysis 23, 169–176. https://doi.org/10.1002/elan.201000419.

Sharma, S., Byrne, H., O'Kennedy, R.J., 2016. Essays Biochem. 60, 9–18. https://doi.org/10.1042/EBC20150002.

Singh, R., Gupta, R., Bansal, D., Bhateria, R., Sharma, M., 2024. ACS Omega 9, 7336–7356. https://doi.org/10.1021/acsomega.3c08060.

Tabatabaei, M.S., Ahmed, M., 2022. Cancer Cell Biology: Methods and Protocols. Springer US, New York, NY, pp. 115–134. https://doi.org/10.1007/978-1-0716-2376-3_10.

Tajima, N., Takai, M., Ishihara, K., 2011. Anal. Chem. 83, 1969–1976. https://doi.org/10.1021/ac1026786.

Thenmozhi, K., Narayanan, S.S., 2017. Mater. Sci. Eng. C 70, 223–230. https://doi.org/10.1016/j.msec.2016.08.075.

Tian, L., Cai, L., Ding, Z., Zhou, Y., Zhang, Y., Liu, Q., Ge, X., Yu, C., 2024. Microchem. J. 200, 110417. https://doi.org/10.1016/j.microc.2024.110417.

Timilsina, S.S., Ramasamy, M., Durr, N., Ahmad, R., Jolly, P., Ingber, D.E., 2022. Adv. Healthcare Mater. 11, 2200589. https://doi.org/10.1002/adhm.202200589.

Treccani, S., Bonadies, I., Ferruti, P., Alongi, J., Scarpa, E., Laurienzo, P., Raucci, M.G., Fasolino, I., Ranucci, E., 2025. Biomater. Adv 177, 214415. https://doi.org/10.1016/j.bioadv.2025.214415.

Upadhyay, A.K., Peng, Y.-Y., Chen, S.-M., 2009a. Sens. Actuators, B Chem. 141, 557–565. https://doi.org/10.1016/j.snb.2009.07.025.

Upadhyay, A.K., Ting, T.-W., Chen, S.-M., 2009b. Talanta 79, 38–45. https://doi.org/10.1016/j.talanta.2009.03.010.

Valverde, A., ben Hassine, A., Serafín, V., Muñoz-San Martín, C., Pedrero, M., Garranzo-Asensio, M., Gamella, M., Raouafi, N., Barderas, R., Yáñez-Sedeño, P., Campuzano, S., Pingarrón, J.M., 2020. Electroanalysis 32, 706–714. https://doi.org/10.1002/elan.201900506.

Zhang, D., Li, W., Ma, Z., Han, H., 2019. Biosens. Bioelectron. 126, 800–805. https://doi.org/10.1016/j.bios.2018.11.038.